

# Improved mechanical and thermomechanical properties of alumina substrate via iron doping

Riko. I Made,<sup>a,\*</sup> Eric Jian Rong Phua,<sup>a,b</sup> Stevin Snellius Pramana,<sup>a,c</sup> Chee Cheong Wong,<sup>a</sup> Zhong Chen,<sup>a</sup> Alfred Iing Yoong Tok<sup>a</sup> and Chee Lip Gan<sup>a,\*</sup>

<sup>a</sup>*School of Materials Science and Engineering, Nanyang Technological University, 50 Nanyang Avenue, Singapore 639798, Singapore*

<sup>b</sup>*Institute of Microelectronics, Agency for Science, Technology and Research (A\*STAR), 11 Science Park Road, Singapore Science Park II, Singapore 117685, Singapore*

<sup>c</sup>*Facility for Analysis, Characterization, Testing and Simulation, Nanyang Technological University, 50 Nanyang Avenue, Singapore 639798, Singapore*

Received 25 October 2012; accepted 8 February 2013

Available online 21 February 2013

We present a method to improve the overall properties of sintered alumina substrate via iron doping that has a higher fracture toughness, lower thermal conductivity, lower thermal expansion coefficient and comparable dielectric constant than pure alumina. Such properties are beneficial for harsh environment electronic packages. X-ray and electron probe microanalyses concluded that toughening is likely caused by multiple phase strengthening and ruled out crack bridging or grain boundary strengthening. © 2013 Acta Materialia Inc. Published by Elsevier Ltd. All rights reserved.

**Keywords:** Ceramics; High temperature; Harsh environment; Electronics packaging; High pressure

Harsh environment applications typically use low power devices that do not generate much heat to be dissipated to the environment. On the contrary, it is necessary to prevent heat transfer from the environment to the device chip. For this purpose, a low thermal conductivity substrate is most suitable.

In this study, Al<sub>2</sub>O<sub>3</sub> is selected mainly due to its low thermal conductivity, suitable electrical conducting properties and chemical stability at high temperature; it also has a particularly mature technology and is inexpensive to produce or acquire. However, it has a relatively high dielectric constant and high coefficient of thermal expansion (CTE) than Si, which may impose some reliability concerns.

Iron has been identified as a possible dopant for alumina substrates for such an application. Fe doping has been reported to decrease the transformation temperature of the amorphous alumina  $\eta$  phase to the crystalline  $\alpha$  alumina [1], to possibly improve alumina–metal adhesion [2] and to improve the alumina's fracture toughness by means of a crack-bridging mechanism due to the presence of a ductile iron phase [1,3–5]. However, the

presence of a ductile iron phase may compromise the substrate's electrical insulating properties. On the other hand, having fully oxidized Fe may not lead to strengthening by a crack-bridging mechanism but may deteriorate the alumina's mechanical properties. In this work, we present systematical characterizations of the iron doped alumina substrate produced by powder methods.

A mixture of alumina with 10 wt.% iron (Fe) was prepared by wet ball milling in an alumina jar for 24 h with a 20:1 weight ratio of ball to powder. The resulting powder was uniaxially pressed to form pellets, followed by 200 MPa cold isostatic pressing. The resulting pellets were air sintered at 1500 °C for 12 h.

The fracture toughness of the sample was deduced from the crack length measurement from Vickers indentation based on the following relation [6]:

$$K_c = \xi_v^R (E/H)^{1/2} (P/c_o^{3/2}) \quad (1)$$

where  $P$  is the indentation peak load,  $c_o$  is the crack length,  $\xi_v^R = 0.016 \pm 0.004$  is a material-independent constant for Vickers-produced radial cracks [6],  $E$  is the Young's modulus and  $H$  is the materials hardness, defined as

$$H = P/a_o a^2 \quad (2)$$

\* Corresponding authors. Tel.: +65 6790 5909 (Chee Lip Gan); e-mail addresses: [imaderiko@ntu.edu.sg](mailto:imaderiko@ntu.edu.sg); [clgan@ntu.edu.sg](mailto:clgan@ntu.edu.sg)

where  $a$  is the half diagonal of the indentation length and  $a_0 = 2$  is a numerical constant for the Vickers indenter. Sintered samples were indented with a Vicker's pyramid-shaped tip microindenter with 10 kgf load setting for 10 s dwell time. Commercially purchased sintered alumina samples from Xellatech Pte. Ltd. were also measured and used as a reference.

The thermal conductivity of the sintered sample was deduced from the thermal diffusivity measurement by the laser flash method. The thermal diffusivity was indirectly measured by observing the temperature changes on the front side of the sample by laser illumination from the back of the sample. Thus, the thermal conductivity was obtained by the following relation [7]:

$$k = \alpha \rho C \quad (3)$$

where  $\alpha$  is the thermal diffusivity,  $\rho$  is the density and  $C$  is the specific heat of the specimen.

The thermal expansion coefficient was deduced from measured linear dimensions change with respect to increasing heating ( $5^\circ\text{C min}^{-1}$ ) from 20 to  $400^\circ\text{C}$ . Dielectric constant was obtained from impedance measurement of sintered samples at 1 MHz frequency using Agilent 4284 A LCR-Meter.

Powder X-ray diffraction (XRD) using a Bruker D8 Advance diffractometer with  $\text{Cu } K_\alpha$  radiation was used for phase analysis of ball milled and sintered samples. Rietveld refinements [8] were performed for phase quantification from XRD diffraction patterns. The weight percentage of each phase was calculated based on:

$$w_\alpha = \frac{S_\alpha(ZMV)_\alpha}{\sum_i S_i(ZMV)_i} \quad (4)$$

where  $w_\alpha$  is the weight fraction of phase  $\alpha$ ,  $S$  is the Rietveld scale factor,  $Z$  is the number of formula units in a unit cell,  $M$  is the molecular mass of the formula unit and  $V$  is the unit cell volume [9].

Field emission electron microscopy (FEI Nova 600i (Nanolab), operating at 5 kV) was used to observe the morphology of the samples. The samples were mirror-polished and carbon coated before the electron probe microanalysis (EPMA) was performed on a JEOL JXA-8530F instrument equipped with five wavelength-dispersive spectrometers. The accelerating voltage and current used were 15 kV and 20 nA, respectively.

Comparisons of particle size between as purchased alumina, iron powder and post-ball-milling alumina with 10 wt.% Fe are given in Figure 1(a)–(c), respectively. It can clearly be seen from the secondary electron microscope imaging that ball milling effectively reduces the particle size of the mixed powder.

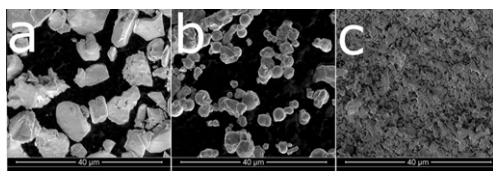


**Figure 1.** Comparison of material particle sizes: (a) raw alumina powder, (b) iron powder, (c) ball-milled mixture of alumina and iron powder.

It was found that Fe-doped samples have a higher fracture toughness ( $6.12 \pm 1.23 \text{ MPa m}^{-0.5}$ ) than undoped reference samples ( $3.14 \pm 0.88 \text{ MPa m}^{-0.5}$ ). The measured absolute density of the doped samples was higher ( $3.83 \pm 0.02 \text{ g cm}^{-3}$ ) than the reference sample ( $3.64 \pm 0.22 \text{ g cm}^{-3}$ ), but both samples have similar relative mass density with respect to their theoretical mixture's density of 10 wt.% Fe ( $4.05 \text{ g cm}^{-3}$ ) and 0 wt.% Fe ( $4.00 \text{ g cm}^{-3}$ ) for the doped and reference sample, respectively.

The doped samples also show a lower thermal diffusivity than the reference sample, i.e.  $5.11 \pm 0.04$  and  $8.14 \pm 0.09 \text{ mm}^2 \text{ s}^{-1}$ , respectively. From differential scanning calorimetry heating and cooling curves, both samples have a heat capacity of  $\sim 0.765 \text{ J g}^{-1} \text{ K}^{-1}$  at  $25^\circ\text{C}$ . Thus, from Eq. (3) we determined that there is a reduction in the thermal conductivity of the doped samples from  $22.43 \pm 0.29$  to  $16.16 \pm 1.91 \text{ W m}^{-1} \text{ K}^{-1}$ .

The doped samples show a CTE reduction from  $8.40 \pm 0.017$  to  $6.91 \pm 0.048 \text{ ppm K}^{-1}$ . On the other hand, the relative dielectric constant is higher for the doped samples than for the reference sample ( $10.36 \pm 0.241$  as compared to  $9.9 \pm 0.018$ ).

XRD characterization of the as-prepared powder, reference and sintered samples are given in Figure 2(a)–(c), respectively. Rietveld refinement of the as-prepared powder shows that around  $2.4 \pm 0.1 \text{ wt.}\%$  crystalline Fe remains in the form of iron metal, hematite ( $\text{Fe}_2\text{O}_3$ ) and wüstite ( $\text{FeO}$ ) from the 10 wt.% Fe initially added. This reduction in the detected quantity of Fe can be attributed to both the formation of amorphous Fe and the addition of alumina. The source of extra alumina could come from erosion debris of the ball milling's jar, as well as from the alumina ball during the ball-milling process. Rietveld refinement also indicated that the average grain size from the integrated breadth volume weighted mean column lengths [10] (LVOL-IB) is  $50 \pm 8 \text{ nm}$ .

On the other hand, the full width at half maximum observed from the XRD patterns of both the reference sample and the sintered samples is narrower than the

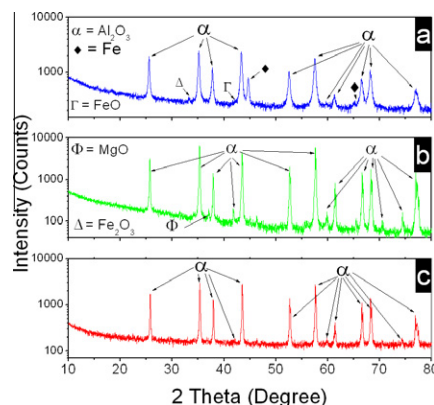


**Figure 2.** XRD of the ball-milled powder, reference sample and sintered sample. (a) Ball-milled powder, consisting of a mixture of  $\text{Al}_2\text{O}_3$ ,  $\text{FeO}$  and  $\text{Fe}_2\text{O}_3$ . After ball milling, only  $2.4 \pm 0.1 \text{ wt.}\%$  Fe is in the mixture. (b) Reference sample, with  $\sim 0.4 \text{ wt.}\%$   $\text{MgO}$  (i.e. trace). (c) Sintered pellet, with  $2.30 \pm 0.04 \text{ at.}\%$  Fe in  $\text{Fe}^{3+}$  found to substitute  $\text{Al}^{3+}$ , equivalent to  $\sim 2.5 \text{ wt.}\%$  Fe.

as-prepared powder XRD pattern. The reference sample shows it consists mostly of alumina with an average grain-size (LVol-IB) of  $128 \pm 11$  nm, with  $\sim 0.4$  wt.% of MgO impurity, which is arguably beyond the XRD detection limit.

All *hkl* reflections can be identified as corundum  $\text{Al}_2\text{O}_3$  phase, with an LVol-IB of  $122 \pm 10$  nm, which is larger than the  $50 \pm 8$  nm of the unsintered powders. Neither crystalline Fe(body-centered cubic, bcc) nor other oxidized Fe was observed. The absence of Fe metal thus implies that the increase in fracture toughness is not caused by a crack-bridging mechanism. Further refinement shows that  $\sim 2.5$  wt.% Fe ( $2.30 \pm 0.04$  at.%) has substituted for  $\text{Al}^{3+}$ . This substitution has expanded the unit cell, with the lattice parameters changing from  $a = 4.7591 \text{ \AA}$  and  $c = 12.9973 \text{ \AA}$  to  $a = 4.7735 \pm 8.8 \times 10^{-4} \text{ \AA}$  and  $c = 13.0293 \pm 3.8 \times 10^{-4} \text{ \AA}$ . No preferred orientation, which may suggest abnormal grain growth, was observed from the refinement. This result indicates that most of the available Fe has been oxidized to  $\text{Fe}^{3+}$  during sintering. The fact that  $\text{Fe}^{3+}$  is preferred over  $\text{Fe}^{2+}$  is due to the ionic radius of  $\text{Fe}^{3+}$  ( $r_{\text{Fe}^{3+}} = 0.49 \text{ \AA}$ ) being closer to that of  $\text{Al}^{3+}$  ( $r_{\text{Al}^{3+}} = 0.39 \text{ \AA}$ ) than the larger  $\text{Fe}^{2+}$  ( $r_{\text{Fe}^{2+}} = 0.63 \text{ \AA}$ ) [11], and the oxygen site is fully occupied within the estimated standard deviation. The amorphization of the iron by ball milling was suspected to be negligible, although further verifications are still needed.

Backscattered electron (BSE) imaging coupled with EPMA was used for the compositional analysis. It reveals that the doped samples consist of three distinct phases, as shown in Figure 3(a), labeled as  $\alpha$ ,  $\beta$  and  $\gamma$ , respectively. The first and darkest phase,  $\alpha$ , consists of around  $99.49 \pm 0.01$  wt.% alumina and  $0.49 \pm 0.01$  wt.%  $\text{Fe}_2\text{O}_3$ . The second phase,  $\beta$ , with a brighter appearance, consists of  $95.02 \pm 0.18$  wt.% alumina and  $4.95 \pm 0.18$  wt.%  $\text{Fe}_2\text{O}_3$ . Finally, the third phase,  $\gamma$ , appears the brightest, and consists of  $59.47 \pm 0.76$  wt.% alumina,  $20.99 \pm 1.10$  wt.%  $\text{Fe}_2\text{O}_3$  and  $19.54 \pm 0.34$  wt.% MgO. Grayscale image analysis of a larger BSE scan (not shown) indicated that the  $\beta$  phase occupies  $\sim 90\%$  of the total area, followed by  $8\%$  of  $\alpha$  and  $0.1\%$  of  $\gamma$  phase.

From the results, the reduction in thermal conductivity is as expected. Introducing Fe as a dopant has effectively created defects in the alumina crystals, which increase the phonon scattering probability, thus reducing the thermal conductivity.

The sources of difference in the CTE can be caused by the difference in porosity, matrix grain size differences or the presence of a second phase. It is clear from the results that doped samples have a higher relative density

than the reference sample, which may also indicate that there is less porosity in the doped sample. However, it has been reported that porosity does not affect the CTE [12]. Furthermore, a higher mass density should lead to a higher CTE, as the thermal motion of the particles has to be accommodated by thermal expansion [13].

A decrease in CTE has been reported in an  $\text{Mg}/\text{Al}_2\text{O}_3$  composite along with a reduction in the grain size [14]. However, the doped and referenced samples were observed to have similar crystallite sizes, of  $120 \pm 10$  and  $128 \pm 11$  nm for doped and reference sample, respectively. Thus, a contribution to CTE reduction by a decrease in grain size can be ruled out.

The presence of a second phase has also been reported to reduce the CTE [13,15,16]. Multiple phases are reported to induce microcracking, which provides the spaces necessary to accommodate the thermal movement of particles without thermal expansion [13]. As observed from the EPMA shown in Figure 3, the doped samples comprise three phases. However, no microcracking was induced. Therefore, the CTE reduction may be attributed to the formation of a second phase. It is not clear how the presence of second and third phases leads to a lower CTE, as the compositing effect of those three phases should produce a CTE in-between those of  $\text{Al}_2\text{O}_3$  and  $\text{Fe}_2\text{O}_3$ , i.e. between  $8.40 \pm 0.017$  and  $9.9 \text{ ppm K}^{-1}$  [17], respectively. Instead, the sintered samples have a CTE of  $6.91 \pm 0.048 \text{ ppm/K}$ , which is lower than both  $\text{Al}_2\text{O}_3$  and  $\text{Fe}_2\text{O}_3$ .

The small increase in dielectric constant could be caused by substitution of  $\text{Fe}^{3+}$  ion for  $\text{Al}^{3+}$ , which induces local charge polarization [18]. By comparing their ionic radii,  $\text{Fe}^{3+}$  is larger than  $\text{Al}^{3+}$  [11], which indicates a stronger attraction of electrons to Al [19]. This tendency may lead to charge polarization of the doped samples; therefore, the doped samples may have slightly higher dielectric constant.

It is well known that the presence of a second phase can improve the fracture toughness of a ceramic [20]. The presence of a ductile phase, in this case Fe, could induce strengthening by means of a crack-bridging mechanism [4]. For this mechanism to work, a sufficient quantity of the ductile phase of Fe metal must be available after sintering. As mentioned earlier, XRD characterization of the sintered samples detected neither Fe(bcc) nor other unoxidized Fe. The absence of Fe thus implies that the increase in fracture toughness is not caused by a crack-bridging mechanism.

Strengthening could also be achieved by an increase in grain size, as coarse grains have been reported to be less susceptible to fracture [21]. It is common to observe an increase in grain size as a result of heat treatment by a mechanism of surface diffusion or bulk diffusion [22], which may lead to higher fracture toughness. Furthermore, an increase in the grain size (possibly inducing abnormal grain growth) might also be enhanced by  $\text{Fe}^{2+}$  diffusion-assisted grain growth [3,23,24].

During sintering,  $\text{Fe}^{2+}$ , which assists the sintering, may become available from pre-existing FeO in the starting powder that loses oxygen atoms or from the oxidation of Fe metal that is available in the mixed powder.  $\text{Fe}_2\text{O}_3$  may not assist the grain growth mechanism

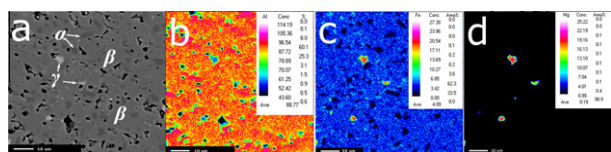


**Figure 3.** BSE scanning electron microscopy coupled with EPMA elemental analysis. (a) Grayscale BSE image showing three distinct phases, i.e.  $\alpha$ ,  $\beta$  and  $\gamma$  phase; (b) Al map; (c) Fe map; (d) Mg map.



much; however, the presence of Fe as a substitute for Al indicates that all Fe and  $\text{Fe}^{2+}$  were eventually oxidized to  $\text{Fe}^{3+}$ , which would diminish  $\text{Fe}^{2+}$ -assisted grain growth [25]. If the oxidation kinetics are slow enough,  $\text{Fe}^{2+}$  may be present during sintering to induce the formation of oxygen vacancies to maintain the charge balance in the crystal. This would lead to faster diffusion paths and thus induce faster grain growth, which would lead to larger grains after sintering [24]. However, the crystallite size of the doped samples and the reference sample are similar, which means that there was little  $\text{Fe}^{2+}$ -enhanced grain growth, hence grain-size-induced toughening was ruled out.

On the other hand, the toughening mechanism could be induced from the presence of non-ductile phases, as presented in Figure 3, i.e.  $\alpha$ ,  $\beta$  and  $\gamma$  phases. The boundary between phases in some circumstances could act to arrest a crack, thus increasing the fracture toughness. Comparing BSE and XRD characterizations, it is understandable that  $\gamma$  phase was not detected by the XRD scan due to its small quantity. However, from EPMA characterizations, we can deduce that the weight concentration of  $\gamma$  corresponds to an atomic ratio of 1.78:0.4:0.74:4 for Al:Fe:Mg:O, respectively. From this, we can roughly deduce that  $\gamma$  has the crystallochemical formula  $[\text{Mg}_{0.74}\text{Fe}^{2+}_{0.22}\square_{0.04}][\text{Al}_{1.78}\text{Fe}^{3+}_{0.18}\square_{0.04}]\text{O}_4$ , which could easily be magnesium aluminate spinel, with some  $\text{Mg}^{2+}$  substituted by  $\text{Fe}^{2+}$  and  $\text{Al}^{3+}$  by  $\text{Fe}^{3+}$  with possible vacancies ( $\square$ ) at both sites. The existence of  $\gamma$  phase has also been observed in the co-doping of alumina with MgO and FeO [26]. By comparing the Fe weight compositions from the EPMA and XRD characterizations, we can deduce that there could be around ~0.98 wt.% amorphous Fe phase; the argument that there is no amorphous Fe induced by ball milling would thus be within experimental error.

Assuming that the quantity of amorphous Fe is negligible, the relative density of the doped sample needs to be calculated based on 2.5 wt.% Fe, as deduced from the XRD characterization, instead of the 10 wt.% Fe of the initial mixture. The corrected relative density for the doped sample would then be  $94.5 \pm 0.06\%$ , which is higher than the reference sample.

The presence of MgO in the sintered samples is unexpected but understandable. A small quantity of MgO has been known to be used as an alumina sintering additive to suppress abnormal grain growth in the alumina, thus improving the final density [27]. From the EPMA results, we could also deduce that the diffraction pattern in the XRD characterization was mostly due to  $\beta$  phase (as shown in Fig. 3a), which occupies ~90% of the scanned area. A ~10% composition by volume may be sufficient to induce the crack-arrest mechanism, and therefore increase the apparent fracture toughness.

In summary, we have seen that Fe-doped alumina substrate could potentially be used for harsh environment electronic application. With comparable electrical properties and potentially less CTE mismatch with silicon, the use of Fe-doped alumina could lead to a more

reliable packaging solution. While the reduction in thermal conductivity can be attributed to an increase in phonon scattering, the reduction in CTE and the observed improvement in fracture toughness are most likely caused by multiple phase strengthening.

The authors acknowledge the SERC for supporting this work via Grant No. 1021650081. The authors also acknowledge Dr. S. Valavan, from Republic Polytechnic Singapore, for access to the thermal diffusivity measurement system.

- [1] X. Devaux, C. Laurent, A. Rousset, *Nanostruct. Mater.* 2 (1993) 339.
- [2] R. Kondou, T. Suga, in: *Electronic Components and Technology Conference (ECTC)*, 2011 IEEE 61st, IEEE, Lake Buena Vista, FL, 2011, pp. 2165–2170. <http://dx.doi.org/10.1109/ECTC.2011.5898819>.
- [3] P. Tartaj, J. Tartaj, *Chem. Mater.* 14 (2002) 536.
- [4] P.A. Trusty, J.A. Yeomans, *J. Eur. Ceram. Soc.* 17 (1997) 495.
- [5] J. Guichard, O. Tillement, A. Mocellin, *J. Mater. Sci.* 32 (1997) 4513.
- [6] G.R. Anstis, P. Chantikul, B.R. Lawn, D.B. Marshall, *J. Am. Ceram. Soc.* 64 (1981) 533.
- [7] F. Boey, A.I.Y. Tok, Y.C. Lam, S.Y. Chew, *Mater. Sci. Eng., A* 335 (2002) 281.
- [8] H.M. Rietveld, *J. Appl. Crystallogr.* 2 (1969) 65.
- [9] R.J. Hill, C.J. Howard, *J. Appl. Crystallogr.* 20 (1987) 467–474.
- [10] A.R. Stokes, A.J.C. Wilson, *Math. Proc. Cambridge Philos. Soc.* 38 (1942) 313.
- [11] R.D. Shannon, *Acta Crystallogr. A* 32 (1976) 751.
- [12] R.L. Coble, W.D. Kingery, *J. Am. Ceram. Soc.* 39 (1956) 377–385.
- [13] P. Oikonomou, C. Dedeloudis, C.J. Stournaras, C. Ftikos, *J. Eur. Ceram. Soc.* 27 (2007) 3475.
- [14] S.F. Hassan, M. Gupta, *Compos. Struct.* 72 (2006) 19.
- [15] T. Hsieh, H. Choe, E.J. Lavernia, J. Wolfenstine, *Mater. Lett.* 30 (1997) 407.
- [16] J.J. Meléndez-Martínez, M. Jimenez-Melendo, A. Domínguez-Rodríguez, G. Wötting, *J. Eur. Ceram. Soc.* 21 (2001) 63.
- [17] S.B. Qadri, C. Fahed, H. Kim, A. Piqué, N.A. Mahadik, M.V. Rao, *Phys. Status Solidi B* 248 (2011) 928–930.
- [18] N. Ikeda, H. Ohsumi, K. Ohwada, K. Ishii, T. Inami, K. Kakurai, Y. Murakami, K. Yoshii, S. Mori, Y. Horibe, *Nature* 436 (2005) 1136.
- [19] M. Birkholz, *Z. Phys. B: Condens. Matter* 96 (1995) 333.
- [20] M. Farkash, D. Brandon, *Mater. Sci. Eng., A* 177 (1994) 269.
- [21] S.-J. Cho, B.J. Hockey, B.R. Lawn, S.J. Bennison, *J. Am. Ceram. Soc.* 72 (1989) 1249–1252.
- [22] R.L. Coble, *J. Am. Ceram. Soc.* 41 (1958) 55–62.
- [23] J. Tartaj, G.L. Messing, *J. Eur. Ceram. Soc.* 17 (1997) 719.
- [24] W.R. Rao, I.B. Cutler, *J. Am. Ceram. Soc.* 56 (1973) 588.
- [25] R. Stöber, M. Nofz, M. Feist, G. Scholz, *J. Solid State Chem.* 179 (2006) 652.
- [26] J. Zhao, M.P. Harmer, *J. Am. Ceram. Soc.* 70 (1987) 860.
- [27] S.I. Bae, S. Baik, *J. Am. Ceram. Soc.* 77 (1994) 2499.